ADVANCED MATERIALS INTERFACES
www.advmatinterfaces.de

Aminosilane-Modified $CuGaO_2$ Nanoparticles Incorporated with CuSCN as a Hole-Transport Layer for Efficient and Stable Perovskite Solar Cells

Byungho Lee, Alan Jiwan Yun, Jinhyun Kim, Bumjin Gil, Byungha Shin, and Byungwoo Park**

Herein, solution-processible inorganic hole-transport layer (HTL) of a perovskite solar cell that consists of $CuGaO_2$ nanoparticles and CuSCN, which leads to an improved device performance as well as long-term stability, is reported. Uniform films of $CuGaO_2$ are prepared by first treating $CuGaO_2$ nanoparticles with aminosilane that leads to well-dispersed $CuGaO_2$ solution, followed by spin-coating of the suspension. Subsequent spin-coating of CuSCN solution onto the $CuGaO_2$ forms a smooth HTL with excellent coverage and electrical conductivity. Comparing to the reference device with CuSCN HTL, the $CuGaO_2$/CuSCN device improves carrier extraction and reduces trap density by ≈40%, as measured by photoluminescence and capacitance analysis. Excellent thermal stability is also demonstrated: ≈80% of the initial efficiency of the perovskite solar cells with the $CuGaO_2$/CuSCN HTL is retained after 400 h under 85 °C/85% relative humidity environment.

1. Introduction

The record power conversion efficiency (PCE) of a perovskite solar cell has now surpassed those of other single-junction thin film solar cells such as CdTe and $Cu(In,Ga)Se_2$, approaching closer to the Shockley–Queisser theoretical limit owing to its superior physical properties.[1–6] However, one of the remaining challenges for commercializing the perovskite solar cells is relatively poor long-term stability.[7–10] Perovskite films tend to degrade into a hydrate form in humid atmosphere, and decompose into PbI_2 in the presence of oxygen under illumination via the reaction with superoxide.[11–13] Many strategies have been proposed to mitigate the intrinsic degradation of perovskite films, and they include augmentation of grain size and alloying of cations with Cs or Rb and anions with Br.[14–17] Another approach involves encapsulation of the devices that prevents O_2 and H_2O in the atmosphere from interacting with the perovskite films. However, thermal stress, which is one of the main factors affecting stability, is still an issue even for well-encapsulated devices. Not only does thermal stress degrade perovskite films, but also it can damage 2,2′,7,7′-tetrakis-(N,N-di-4-methoxyphenylamino)-9,9′-spirobifluorene (spiro-OMeTAD), one of the most common hole-transport layers (HTLs) used in high-performing perovskite solar cells.[18–21] To improve the electrical conductivity of spiro-OMeTAD, it is common to incorporate dopant additives such as lithium bis(trifluoromethanesulfonyl)imide (Li-TFSI) and 4-*tert*-butylpyridine (TBP) to spiro-OMeTAD. When a doped spiro-OMeTAD layer is subjected to a temperature above 85 °C, pinholes begin to form in the film, leading to the deterioration of device performance.[19–21] As a remedy, polymer-modified spiro-OMeTAD has recently been introduced and demonstrated some success in improving the long-term thermal stability.[22] Still, the use of costly organic hole-transport materials is ultimately not desirable for the commercialization.[23–25]

Intrinsic thermal instability of organic charge-transport layers leads to serious research efforts on the inorganic HTLs.[26–34] Among the potential candidates as an inorganic HTL, CuSCN is an attractive choice because it is cheap and solution-processible with solvents such as diethyl sulfide and dipropyl sulfide.[24,25,30,34] Although the thermal stability of a CuSCN layer itself is excellent, it is known to react with the underlying perovskite to form PbI_2 and CuI impurities when the layers are subjected to a temperature above 85 °C.[34] In order to reduce the interfacial reaction between CuSCN HTL and a perovskite layer, Snaith and co-workers have inserted a mesoporous layer of Al_2O_3 nanoparticles before the CuSCN

Dr. B. Lee, A. J. Yun, Dr. J. Kim, B. Gil, Prof. B. Park
Department of Materials Science and Engineering
Research Institute of Advanced Materials
Seoul National University
Seoul 08826, Korea
E-mail: byungwoo@snu.ac.kr
Prof. B. Shin
Department of Materials Science and Engineering
Korea Advanced Institute of Science and Technology
Daejeon 34141, Korea
E-mail: byungha@kaist.ac.kr
The ORCID identification number(s) for the author(s) of this article can be found under https://doi.org/10.1002/admi.201901372.

© 2019 The Authors. Published by WILEY-VCH Verlag GmbH & Co. KGaA, Weinheim. This is an open access article under the terms of the Creative Commons Attribution License, which permits use, distribution and reproduction in any medium, provided the original work is properly cited.
The copyright line for this article was changed on 8 November 2019 after original online publication.

DOI: 10.1002/admi.201901372

deposition and have demonstrated improved thermal stability of the devices.[34] However, insulating Al_2O_3 can impede hole extraction to HTL from the perovskite, giving rise to the reduction of the photovoltaic performance. It is then expected that a thin layer of conductive metal oxide in place of the Al_2O_3 will improve thermal stability without sacrificing PCE. One of the promising candidates for the conductive metal oxide layer is $CuGaO_2$ because it has a high mobility (≈0.1 $cm^2\ V^{-1}\ s^{-1}$) and favorable valence-band maximum (–5.3 eV vs vacuum level) to form a junction with perovskite.[35] Deposition of $CuGaO_2$ thin films by vacuum process such as sputter or pulsed laser deposition (PLD) at a temperature below 500 °C results in Cu_2O or $CuGa_2O_4$ impurities.[36,37] On the other hand, spin-coating a suspension of presynthesized $CuGaO_2$ nanoparticles in a solvent is a facile method to deposit phase-pure thin films. However, preparing a uniform $CuGaO_2$ film with a full coverage by solution process is difficult due to the agglomeration of $CuGaO_2$ nanoparticles in suspension.

Herein, $CuGaO_2$ nanoparticles are used for the HTL with CuSCN in *n-i-p* structured cells to enhance both PCE and thermal stability. The surface of $CuGaO_2$ nanoparticles is modified by (3-aminopropyl)triethoxysilane (APTES) to reduce the agglomeration of nanoparticles, resulting in a substantial improvement in the uniformity of nanoparticle films. Compared to the HTL consisting of only CuSCN or $CuGaO_2$, a $CuGaO_2$/CuSCN HTL stack exhibits more efficient carrier extraction. Also, trap density of the solar cell using $CuGaO_2$ with CuSCN is reduced by ≈40% compared to the reference with only CuSCN, leading to the enhanced PCE. Moreover, an excellent thermal stability of the perovskite solar cells is demonstrated: ≈80% of the initial PCE retention after 400 h under 85 °C/85% relative humidity (RH) condition (encapsulated).

2. Results and Discussion

In order to prepare the metal-oxide HTL with a high coverage, controlling the nanoparticle size is important. We have used P123 as a surfactant in the hydrothermal synthesis to reduce the $CuGaO_2$ particle size below 100 nm. X-ray diffraction (XRD) from the synthesized $CuGaO_2$ nanoparticles exhibits peaks corresponding to $CuGaO_2$ without impurity phases, confirming high purity of the $CuGaO_2$ nanoparticles (**Figure 1**a). The grain size is ≈5 nm along the ⟨001⟩ direction and ≈35 nm for the ⟨110⟩ direction, as calculated by the Scherrer equation suggesting plate-shaped nanoparticles. To enhance the dispersion property of the nanoparticles in a solvent, APTES treatment is conducted (details in the Experimental Section). During the APTES treatment, hydroxyl groups on the nanoparticle surface are replaced by the silane groups of APTES, and the amine groups are exposed causing repulsive force between the nanoparticles, therefore enhancing their dispersion. The comparison of Fourier transform infrared (FTIR) spectra from $CuGaO_2$ nanoparticles before and after the APTES treatment reveals that Cu–O–Si vibration peak (980 cm^{-1}) appears after the APTES treatment with the disappearance of –OH groups

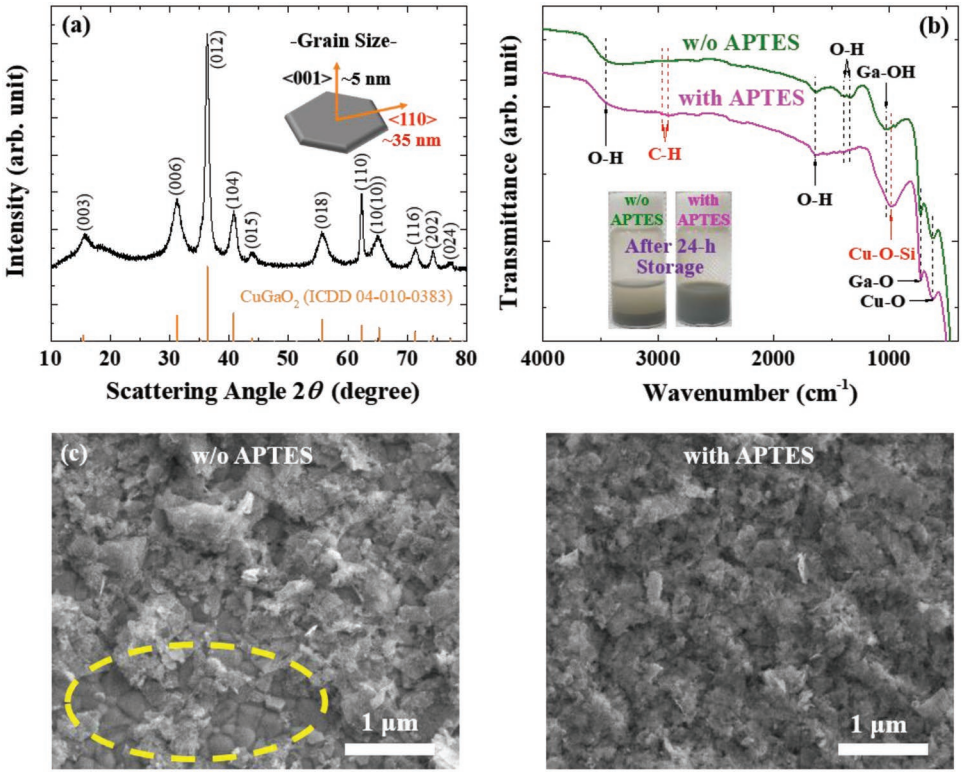

Figure 1. The effect of APTES treatment on the $CuGaO_2$-nanoparticle nanostructures. a) X-ray diffraction of $CuGaO_2$ nanoparticles, and extracted grain size by Scherrer equation. b) FTIR of $CuGaO_2$ nanoparticles. The inset shows optical images of nanoparticle suspension after 24 h storage with and w/o APTES treatment. c) Coverage of $CuGaO_2$ films on the perovskite by SEM. A yellow circle indicates exposed perovskite.

© 2019 The Authors. Published by WILEY-VCH Verlag GmbH & Co. KGaA, Weinheim

(1337 and 1387 cm^{-1}), as shown in Figure 1b.[31,38–40] This confirms that APTES becomes chemically adsorbed on the $CuGaO_2$ nanoparticles via the silane group. It is noted that the vibrational modes of P123 surfactant used in the hydrothermal process are not observed confirming the complete removal of P123 after the washing step.

Even after storage for 24 h without stirring under ambient air, $CuGaO_2$ nanoparticles in isopropyl alcohol (IPA) maintain their dispersion with APTES treatment (inset of Figure 1b). $CuGaO_2$ film is deposited on the perovskite by spin-coating (Figure 1c). Without the APTES treatment, a low-coverage $CuGaO_2$ film is resulted exposing some areas of the underlying perovskite film (yellow circle). On the other hand, a full coverage film is obtained with the APTES-treated $CuGaO_2$ nanoparticles. Although the APTES treatment enhances the dispersion of nanoparticles in suspension, careful adjustment of the treatment time is necessary so that the formation of multilayer APTES can be avoided: Otherwise, electrical conductivity can decrease. The optimal treatment time is determined by in-plane conductivity measurements (Figure S1, Supporting Information).

Solar cells comprised of SnO_2 as an electron-transport layer, triple-cation perovskite $[Cs_{0.05}(FA_{0.83}MA_{0.17})_{0.95}Pb(I_{0.83}Br_{0.17})_3]$ as a light absorber, and either CuSCN or $CuGaO_2$ with CuSCN ($CuGaO_2$/CuSCN) as HTLs are fabricated (**Figure 2**a). The $CuGaO_2$/CuSCN HTL is prepared by spin-coating $CuGaO_2$ suspension, followed by spin-coating CuSCN solution. The schematic configuration of the solar cell with the expected energy-level diagram for each component is shown in Figure S2 (Supporting Information).[30,35,41–43] The photogenerated electrons in the perovskite absorber can be transferred to the SnO_2 electron-transport layer, whereas holes can be transferred to the $CuGaO_2$ or CuSCN. The holes injected into the $CuGaO_2$ can be further transferred to the CuSCN, considering the energy-level diagram. As shown in Figure S3 (Supporting Information), the surface topography varies significantly depending on the types of HTLs. The root-mean-squared (RMS) roughness of the perovskite is 17.8 nm, and it is reduced to 7.4 nm after the deposition of CuSCN. For the $CuGaO_2$-only HTL on perovskite, the RMS roughness exhibits the highest value of 40.9 nm, and it is reduced to 31.4 nm for the $CuGaO_2$/CuSCN device, indicating that the CuSCN solution can infiltrate into a porous

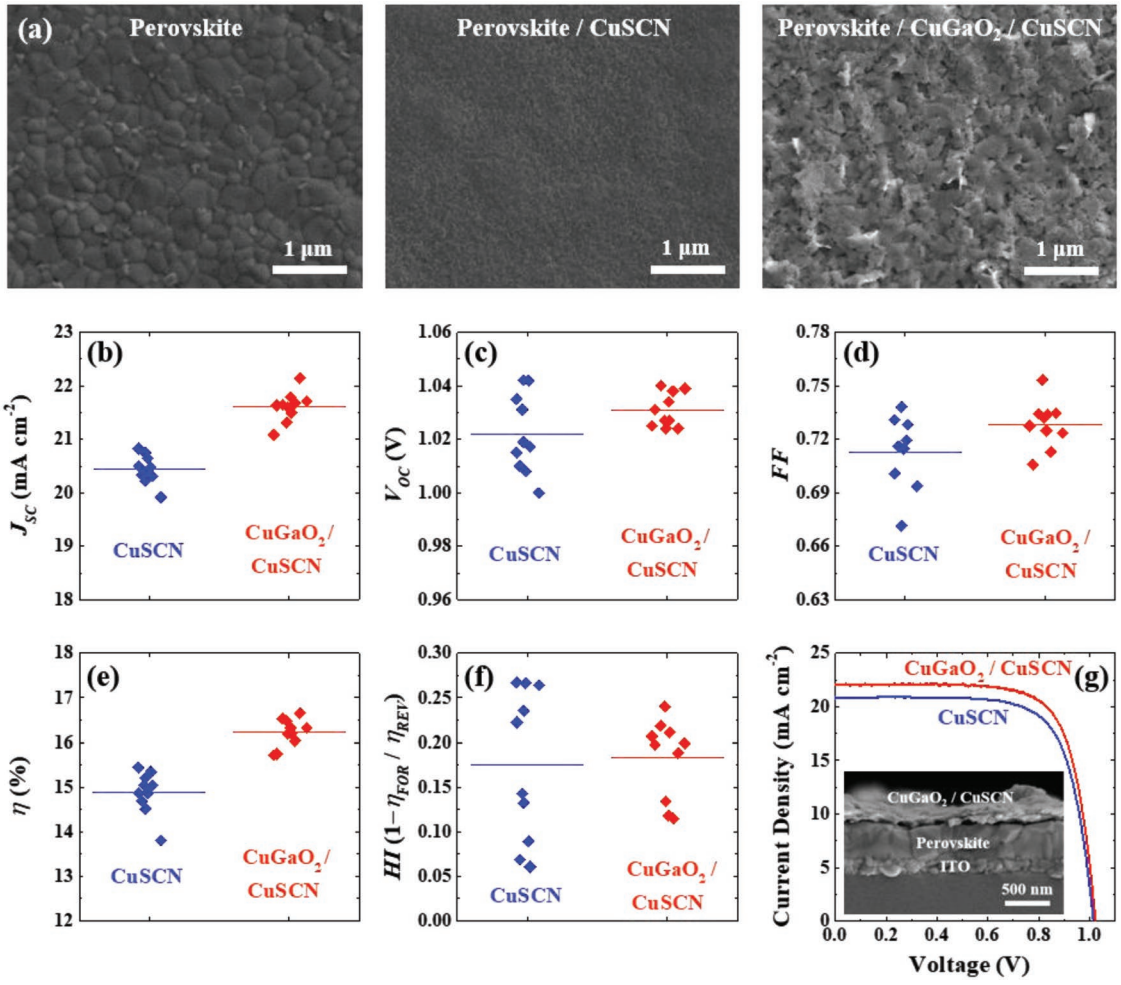

Figure 2. Device performance without and with nanoparticles for the HTL. a) Morphologies of perovskite, perovskite/CuSCN, and perovskite/$CuGaO_2$/CuSCN by SEM. b) J_{SC}, c) V_{OC}, d) FF, e) η, and f) HI = 1 − η_{FOR}/η_{REV} of solar cells with different hole-transport layers. g) *J–V* curves of champion cells with solar cell geometry (without Au) by SEM.

© 2019 The Authors. Published by WILEY-VCH Verlag GmbH & Co. KGaA, Weinheim

Table 1. Photovoltaic parameters of the solar cells (reverse scans for ten cells). Devices without and with $CuGaO_2$ nanoparticles for the HTL. The data in the parentheses are from the highest efficient devices. HI, η_{FOR}, and η_{REV} are the hysteresis index, average photovoltaic efficiencies at forward and reverse scans, respectively.

Sample	J_{sc} [mA cm^{-2}]	V_{oc} [V]	FF	η [%]	HI [$1-\eta_{FOR}/\eta_{REV}$]
CuSCN	20.4 ± 0.3 (20.8)	1.02 ± 0.01 (1.02)	0.71 ± 0.02 (0.73)	14.9 ± 0.4 (15.4)	0.18
$CuGaO_2$/CuSCN	21.6 ± 0.3 (22.1)	1.03 ± 0.01 (1.02)	0.73 ± 0.01 (0.74)	16.2 ± 0.3 (16.7)	0.18

$CuGaO_2$ film reducing pinholes and roughnesses. The in-plane conductivity of the $CuGaO_2$ film is not improved by the infiltrated CuSCN because the conductivity of the bare CuSCN is lower by more than an order of magnitude compared to the $CuGaO_2$ film (Figure S4, Supporting Information). The average performance of solar cells with $CuGaO_2$/CuSCN HTL improves compared to the CuSCN-only HTL (Figure 2b–f and **Table 1**). Photocurrent–voltage (*J*–*V*) curves of the best-performing cells are shown in Figure 2g (improved PCE of 16.7% from 15.4%). Shown in the inset of Figure 2g is a cross-sectional scanning electron microscope (SEM) image of the solar cell with the $CuGaO_2$/CuSCN HTL which suggests a uniform layer of $CuGaO_2$ infiltrated with CuSCN, instead of distinct bilayers of separate $CuGaO_2$ and CuSCN. The optimum thicknesses of CuSCN-only and $CuGaO_2$/CuSCN HTL are ≈90 and ≈170 nm, respectively (Figures S5 and S6, Supporting Information). The standard deviation of PCE for each device is less than 0.4% exhibiting outstanding reproducibility of our optimal devices (Table 1). As shown in Figure 2f, both devices using CuSCN-only or $CuGaO_2$/CuSCN HTL exhibit similar average hysteresis indices (HI = $1 - \eta_{FOR}/\eta_{REV}$). The main parameters affecting the hysteresis are V_{OC} and FF for both devices (Figure S7, Supporting Information). The analogous behavior of the devices suggests that the properties of bulk perovskite and/or *n*-type electrode rather than those of the perovskite/HTL interfaces may dominantly affect the hysteresis, and detailed study of the cause of hysteresis is necessary as a future work. It is noted that PCE of a solar cell with $CuGaO_2$-only HTL is lower than 4% due to the limited contact area between perovskite and $CuGaO_2$ nanoparticles, causing potential shunting path from pinholes in the $CuGaO_2$ layer (Figure S1, Supporting Information).[44]

To better understand the reasons of the performance enhancement with the $CuGaO_2$/CuSCN HTL, photoluminescence (PL) analysis is carried out. For steady-state PL measurements, the excitation light is incident on the HTL side to probe the perovskite/HTL interface better. The PL intensity of the perovskite is substantially quenched with the presence of a HTL. However, the degree of the quench is larger for the $CuGaO_2$/CuSCN compared to the CuSCN-only one (**Figure 3**a). It is noted that the PL peak position of the perovskite is close to the estimated optical bandgap (1.63 eV), that is, very small Stokes shift, suggesting the high quality of perovskite film,[45] and the blueshifted PL after the deposition of HTL suggests that additional defects are not generated at the perovskite/HTL interface.

The efficacy of carrier extraction across the perovskite/HTL is examined by time-resolved PL spectra (Figure 3b). Unlike the steady-state PL measurements, the excitation light is incident on the glass side to simulate the illumination condition identical to the solar-cell operation. The PL lifetimes are ≈291, 17, and 10 ns, respectively, for glass/perovskite, glass/perovskite/CuSCN, and glass/perovskite/$CuGaO_2$/CuSCN.[46] The reduced PL lifetime can be attributed to the efficient hole extraction from the perovskite to the HTL. When only $CuGaO_2$ is used for the HTL, carrier extraction is less efficient compared to the $CuGaO_2$/CuSCN owing to the insufficient contact area between the perovskite and the $CuGaO_2$ (Figure S8, Supporting Information). The better hole extraction for the $CuGaO_2$/CuSCN HTL compared to the only CuSCN or $CuGaO_2$ HTL suggests that the infiltrated CuSCN into the porous $CuGaO_2$ nanoparticle film enhances hole transfer from the perovskite. More efficient charge extraction between the perovskite and $CuGaO_2$/CuSCN HTL can also be inferred by the improved external quantum efficiency (EQE) response over the nearly entire wavelength range in which the solar cells respond (Figure 3c). Additionally, the plot for the ratio of $EQE_{CuGaO2/CuSCN}$ to EQE_{CuSCN} shows better EQE response at longer wavelength with the $CuGaO_2$/CuSCN device, indicating improved hole carrier collection (Figure 3d).

Capacitance measurements of solar cells using two different HTLs exhibit a similar high-frequency plateau but different response in a low-frequency range (**Figure 4**a). The high-frequency value can be attributed to the geometric/depletion capacitances, while the disparity in the low-frequency range can be ascribed to the difference in the trap density at the perovskite and/or interfaces.[42,47,48] The trap density can be estimated using the derivative of the capacitance with respect to the frequency, and the corresponding trap level with respect to the bandedge is related to the applied angular frequency.[42,47,48] The resultant distributions of trap density exhibit lower integrated trap density (by a Gaussian fitting) for the $CuGaO_2$/CuSCN device compared to the CuSCN-only device (Figure 4b). Therefore, it is deduced that wetting by CuSCN through the $CuGaO_2$ nanoparticles may suppress or passivate surface/interface trap states.

The stability of a perovskite solar cell is evaluated under 85 °C/85% RH environment (Figure 4c). A much improved thermal stability is confirmed with the $CuGaO_2$/CuSCN HTL: almost 80% of the initial PCE retention after 400 h. To investigate the effect of $CuGaO_2$ layer on the degradation between perovskite and CuSCN, perovskite films with each HTL (encapsulated by using poly(methyl methacrylate) (PMMA)) before and after storage at 85 °C for 100 h are analyzed by XRD (Figure S9, Supporting Information). We have compared the integrated-intensity ratios of a pristine sample to a sample after storage at 85 °C for 100 h for the perovskite and PbI_2 peaks. The decomposition of perovskite and the formation of PbI_2 are accelerated with the CuSCN compared to the bare perovskite film. The interfacial reaction between perovskite and CuSCN may aggravate the device stability at high temperature.[34] The

© 2019 The Authors. Published by WILEY-VCH Verlag GmbH & Co. KGaA, Weinheim

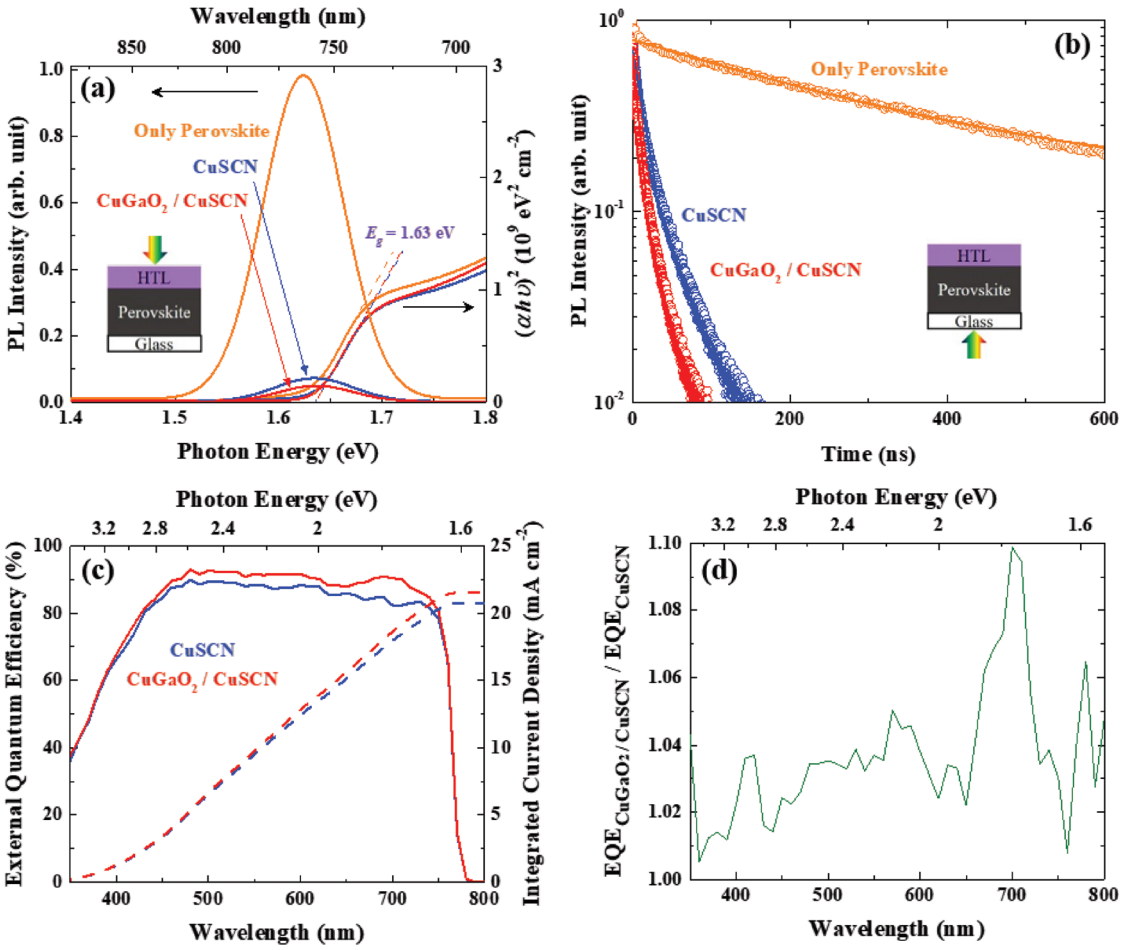

Figure 3. Carrier extraction properties. a) Steady-state PL spectra (excitation wavelength = 532 nm) and plots of $(\alpha h\upsilon)^2$ versus $h\upsilon$ for the estimation of optical bandgap (E_g) of perovskite before/after the deposition of HTL. b) Time-resolved PL spectra with solid fitting lines (excitation wavelength = 405 nm). c) External quantum efficiencies (EQEs) of the solar cells. d) The ratio of $EQE_{CuGaO_2/CuSCN}$ to EQE_{CuSCN} as a function of wavelength.

degradation is mitigated by using $CuGaO_2$ with CuSCN, which can be ascribed to the reduced contact area between perovskite and CuSCN.

Recently, Seok and co-workers have reported thermal stability of CuSCN-based perovskite solar cells, and the efficiency of their device rapidly degraded to ≈60% of the initial value (η = 18%) during the first 2 h at 125 °C.[49] Grätzel and co-workers have reported PCE exceeding 20% and the operational stability retaining ≈95% of initial value at 60 °C under illumination for 1000 h.[24] Although our devices show lower PCE than

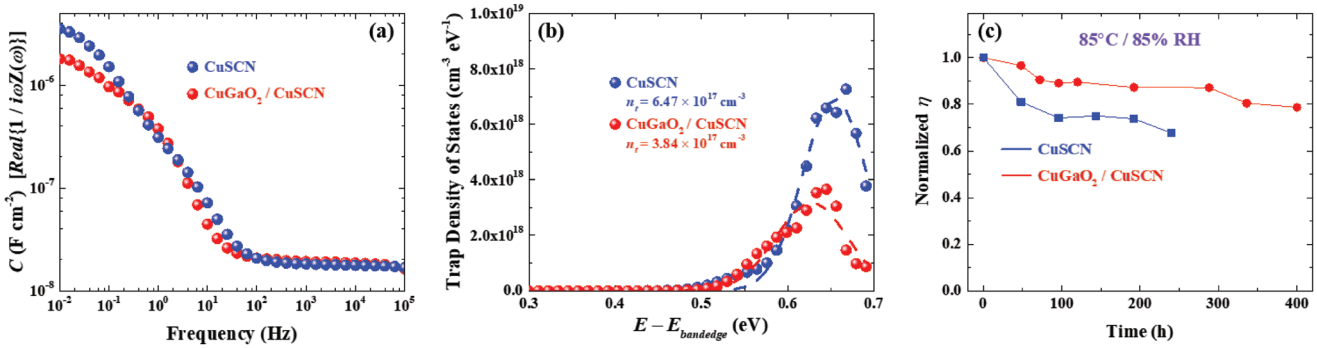

Figure 4. Trap density analysis and stability of the devices. a) Frequency-dependent capacitances. b) Trap density of states as a function of trap level with respect to the bandedge. The dashed lines denote Gaussian fitting for the trap density per volume (n_t). c) Stability test of solar cells in 85 °C/85% relative humidity (RH) condition with encapsulation.

© 2019 The Authors. Published by WILEY-VCH Verlag GmbH & Co. KGaA, Weinheim

the reported values, we have shown that the interfacial *p*-type oxide layer can improve thermal stability by reducing the degradation reactions between the perovskite and CuSCN. Our findings emphasize that the mitigation of interfacial degradation is a key to improve the thermal stability of the perovskite solar cells.

3. Conclusions

We have fabricated perovskite solar cells with inorganic HTL consisting of $CuGaO_2$ nanoparticle film and CuSCN to improve the thermal stability of devices. First, the dispersion of $CuGaO_2$ nanoparticles in the suspension is enhanced by the surface modification of nanoparticles with aminosilane groups by APTES. After treatment, the resultant $CuGaO_2$ suspension is effectively spin-coated yielding films with better coverage and uniformity. The HTL with a dual-inorganic layer $CuGaO_2$/CuSCN shows more efficient carrier extraction from the underlying perovskite. This leads to the improved EQE response, and therefore, a higher short-circuit current from the $CuGaO_2$/CuSCN solar cell. The trap density is also reduced by ≈40% by the $CuGaO_2$/CuSCN compared to the CuSCN-only case. Consequently, the average PCE for the $CuGaO_2$/CuSCN solar cells is larger than the CuSCN-only solar cells. The encapsulated $CuGaO_2$/CuSCN solar cell maintains ≈80% of its initial PCE for 400 h under 85 °C/85% RH condition. Our study presents an effective strategy that can both improve performance and thermal stability of perovskite solar cells.

4. Experimental Section

Synthesis of $CuGaO_2$ Nanoparticles and APTES Treatment: 7 g of P123 (Sigma-Aldrich) was dissolved in 140 mL of deionized (DI) water by stirring for 4 h at room temperature (RT). Then 2 mmol of $Cu(NO_3)_2{\cdot}2.5H_2O$ (Alfa Aesar) and $Ga(NO_3)_3{\cdot}xH_2O$ (Alfa Aesar), 4 mL of ethylene glycol (Alfa Aesar), and 4.5 mL of 1 M KOH aqueous solution (Daejung) were added sequentially during vigorous stirring. After the solution was stirred for 1 h, the precursor was transferred to 200 mL Teflon-lined stainless-steel autoclave. The sealed autoclave was placed in a preheated oven at 220 °C for 4 h, then cooled under water flow. The synthesized particles were centrifuged and washed with diluted ammonia solution (5 wt%), diluted nitric acid (5 wt%), and DI water for two times, respectively. Then, the particles were additionally washed with ethyl alcohol for three times and isopropyl alcohol (IPA) for five times. For surface modification, 1 vol% of APTES (Sigma-Aldrich) was added to the $CuGaO_2$ suspension in IPA (10 mg mL^{-1}), and stirred for 3 h at 30 °C. After the reaction, the suspension was ultrasonically treated for 2 min, and washed with IPA for three times to remove any physically adsorbed APTES.

Device Fabrication: Indium tin oxide (ITO) glasses were ultrasonically cleaned in acetone, ethanol, and deionized water, followed by a UV–ozone treatment for 15 min. For SnO_2 electron-transport layer, 15 wt% SnO_2 aqueous solution (Alfa Aesar) was diluted in DI water with the volume ratio of 1:4. The solution was spin-coated at 3000 rpm for 30 s, and annealed at 120 °C for 30 min. The 1.3 M precursor solution for the $Cs_{0.05}(FA_{0.83}MA_{0.17})_{0.95}Pb(I_{0.83}Br_{0.17})_3$ perovskite was prepared by dissolving cesium iodide (CsI, TCI Chemicals), formamidinium iodide (FAI, Greatcell Solar), methylammonium bromide (MABr, Greatcell Solar), lead iodide (PbI_2, TCI Chemicals), and lead bromide ($PbBr_2$, TCI Chemicals) in a mixture of *N*,*N*-dimethylformamide (DMF, Sigma-Aldrich) and dimethyl sulfoxide (DMSO, Sigma-Aldrich) with the volume ratio of 4:1. The solution was deposited onto the substrate by spin-coating at 5000 rpm for 20 s, and 300 µL of chlorobenzene was dripped at 17 s during the spinning process. Then, the film was annealed at 100 °C for 45 min. For the $CuGaO_2$ hole-transport layers, $CuGaO_2$ suspension in IPA (20 mg mL^{-1}) was used for spin-coating at 3000 rpm for 30 s. The spin-coating was conducted for two times, then the film was annealed at 100 °C for 5 min. To deposit CuSCN film (for both CuSCN-only and $CuGaO_2$/CuSCN), CuSCN solution in diethyl sulfide (24 mg mL^{-1}) was used for spin-coating at 3000 rpm for 30 s, and annealed at 50 °C for 10 min. Finally, 150-nm-thick Au electrodes were deposited by thermal evaporation. For the stability test, devices were encapsulated using cover glass with UV-curable epoxy resin in a glovebox.

Characterization: The crystal structure and grain size of $CuGaO_2$ nanoparticles were analyzed by XRD (D8 Advance: Bruker). FTIR spectroscopy (TENSOR27: Bruker) was carried out to observe vibrational modes of chemical bonding in $CuGaO_2$ nanoparticles. The morphologies of the films were observed using a field-emission scanning electron microscope (FESEM, Merlin-Compact: Carl Zeiss). The surface topography of the film was obtained by atomic force microscopy (NX-10: Park Systems). The absorbance was obtained by a UV–vis spectrophotometer (V-770: JASCO). Steady-state and time-resolved photoluminescence spectra were observed in the films prepared on glass substrates with excitation wavelength of 532 and 405 nm (LabRAM HV Evolution: Horiba, FluoTime 300: Picoquant), respectively. The photocurrent–voltage (*J*–*V*) curves of the solar cells were measured using a solar cell measurement system (K3000: McScience, AM 1.5G, 100 mW cm^{-2}), with an active area of 0.09 cm^2 and 100 mV s^{-1} voltage scan rate. The EQE spectra were obtained by an incident photon-to-current conversion efficiency (IPCE) measurement system (K3100: McScience). Frequency-dependent capacitances were obtained by impedance analysis in dark condition using a potentiostat (Zive SP1: WonATech Co., Ltd.) with 50 mV amplitude of ac signal at zero applied bias and frequency ranging from 0.01 to 10^5 Hz.

Supporting Information

Supporting Information is available from the Wiley Online Library or from the author.

Acknowledgements

This work was supported by the Korea Institute of Energy Technology Evaluation and Planning (KETEP: 20183010014470).

Conflict of Interest

The authors declare no conflict of interest.

Keywords

$CuGaO_2$, CuSCN, long-term stability, perovskite solar cells

Received: August 7, 2019
Revised: September 1, 2019
Published online:

[1] A. Polman, M. Knight, E. C. Garnett, B. Ehrler, W. C. Sinke, *Science* **2016**, *352*, aad4424.
[2] N. J. Jeon, H. Na, E. H. Jung, T.-Y. Yang, Y. G. Lee, G. Kim, H.-W. Shin, S. I. Seok, J. Lee, J. Seo, *Nat. Energy* **2018**, *3*, 682.

© 2019 The Authors. Published by WILEY-VCH Verlag GmbH & Co. KGaA, Weinheim

[3] R. Saive, M. Boccard, T. Saenz, S. Yalamanchili, C. R. Bukowsky, P. Jahelka, Z. J. Yu, J. Shi, Z. Holmanb, H. A. Atwater, *Sustainable Energy Fuels* **2017**, *1*, 593.
[4] S. Lee, J. C. Flanagan, J. Kim, A. J. Yun, B. Lee, M. Shim, B. Park, *ACS Appl. Mater. Interfaces* **2019**, *11*, 19104.
[5] H. H. Park, R. Heasley, L. Sun, V. Steinmann, R. Jaramillo, K. Hartman, R. Chakraborty, P. Sinsermsuksakul, D. Chua, T. Buonassisi, R. G. Gordon, *Prog. Photovoltaics* **2015**, *23*, 901.
[6] T. Hwang, D. Cho, J. Kim, J. Kim, S. Lee, B. Lee, K. H. Kim, S. Hong, C. Kim, B. Park, *Nano Energy* **2016**, *25*, 91.
[7] J. Kim, T. Hwang, B. Lee, S. Lee, K. Park, H. H. Park, B. Park, *Small Methods* **2019**, *3*, 1800361.
[8] J. Kim, A. J. Yun, B. Gil, Y. Lee, B. Park, *Adv. Funct. Mater.* **2019**, https://doi.org/10.1002/adfm.201905190.
[9] T. Hwang, B. Lee, J. Kim, S. Lee, B. Gil, A. J. Yun, B. Park, *Adv. Mater.* **2018**, *30*, 1704208.
[10] B. Lee, B. Shin, B. Park, *Electron. Mater. Lett.* **2019**, *15*, 192.
[11] Q. Wang, B. Chen, Y. Liu, Y. Deng, Y. Bai, Q. Dong, J. Huang, *Energy Environ. Sci.* **2017**, *10*, 516.
[12] N. Aristidou, C. Eames, I. Sanchez-Molina, X. Bu, J. Kosco, M. S. Islam, S. A. Haque, *Nat. Commun.* **2017**, *8*, 15218.
[13] N. Aristidou, I. Sanchez-Molina, T. Chotchuangchutchaval, M. Brown, L. Martinez, T. Rath, S. A. Haque, *Angew. Chem., Int. Ed.* **2015**, *54*, 8208.
[14] J. H. Noh, S. H. Im, J. H. Heo, T. N. Mandal, S. I. Seok, *Nano Lett.* **2013**, *13*, 1764.
[15] M. Saliba, T. Matsui, J.-Y. Seo, K. Domanski, J.-P. Correa-Baena, M. K. Nazeeruddin, S. M. Zakeeruddin, W. Tress, A. Abate, A. Hagfeldt, M. Grätzel, *Energy Environ. Sci.* **2016**, *9*, 1989.
[16] T. Matsui, T. Yamamoto, T. Nishihara, R. Morisawa, T. Yokoyama, T. Sekiguchi, T. Negami, *Adv. Mater.* **2019**, *31*, 1806823.
[17] J. Kim, T. Hwang, S. Lee, B. Lee, J. Kim, G. S. Jang, S. Nam, B. Park, *Sci. Rep.* **2016**, *6*, 25648.
[18] T. Leijtens, K. Bush, R. Cheacharoen, R. Beal, A. Bowring, M. D. McGehee, *J. Mater. Chem. A* **2017**, *5*, 11483.
[19] A. K. Jena, M. Ikegami, T. Miyasaka, *ACS Energy Lett.* **2017**, *2*, 1760.
[20] A. K. Jena, Y. Numata, M. Ikegami, T. Miyasaka, *J. Mater. Chem. A* **2018**, *6*, 2219.
[21] J. Zhang, T. Zhang, L. Jiang, U. Bach, Y.-B. Cheng, *ACS Energy Lett.* **2018**, *3*, 1677.
[22] N. Li, S. Tao, Y. Chen, X. Niu, C. K. Onwudinanti, C. Hu, Z. Qiu, Z. Xu, G. Zheng, L. Wang, Y. Zhang, L. Li, H. Liu, Y. Lun, J. Hong, X. Wang, Y. Liu, H. Xie, Y. Gao, Y. Bai, S. Yang, G. Brocks, Q. Chen, H. Zhou, *Nat. Energy* **2019**, *4*, 408.
[23] Z. Yu, L. Sun, *Small Methods* **2018**, *2*, 1700280.
[24] N. Arora, M. I. Dar, A. Hinderhofer, N. Pellet, F. Schreiber, S. M. Zakeeruddin, M. Grätzel, *Science* **2017**, *358*, 768.
[25] I. S. Yang, S. Lee, J. Choi, M. T. Jung, J. Kim, W. I. Lee, *J. Mater. Chem. A* **2019**, *7*, 6028.
[26] Q. Wu, C. Xue, Y. Li, P. Zhou, W. Liu, J. Zhu, S. Dai, C. Zhu, S. Yang, *ACS Appl. Mater. Interfaces* **2015**, *7*, 28466.
[27] P. Nazari, F. Ansari, B. A. Nejand, V. Ahmadi, M. Payandeh, M. Salavati-Niasari, *J. Phys. Chem. C* **2017**, *121*, 21935.
[28] Y. Yang, H. Chen, X. Zheng, X. Meng, T. Zhang, C. Hu, Y. Bai, S. Xiao, S. Yang, *Nano Energy* **2017**, *42*, 322.
[29] S. Akin, Y. Liu, M. I. Dar, S. M. Zakeeruddin, M. Grätzel, S. Turan, S. Sonmezoglu, *J. Mater. Chem. A* **2018**, *6*, 20327.
[30] S. S. Mali, J. V. Patil, H. Kim, R. Luque, C. K. Hong, *Mater. Today* **2019**, *26*, 8.
[31] C. Liu, X. Zhou, S. Chen, X. Zhao, S. Dai, B. Xu, *Adv. Sci.* **2019**, *6*, 1801169.
[32] J. W. Jo, Y. Yoo, T. Jeong, S. J. Ahn, M. J. Ko, *Electron. Mater. Lett.* **2018**, *14*, 657.
[33] B. Gil, A. J. Yun, Y. Lee, J. Kim, B. Lee, B. Park, *Electron. Mater. Lett.* **2019**, *15*, 505.
[34] J. Liu, S. K. Pathak, N. Sakai, R. Sheng, S. Bai, Z. Wang, H. J. Snaith, *Adv. Mater. Interfaces* **2016**, *3*, 1600571.
[35] H. Zhang, H. Wang, W. Chen, A. K.-Y. Jen, *Adv. Mater.* **2017**, *29*, 1604984.
[36] R.-S. Yu, Y.-C. Lee, *Thin Solid Films* **2018**, *646*, 143.
[37] K. Ueda, T. Hase, H. Yanagi, H. Kawazoe, H. Hosono, H. Ohta, M. Orita, M. Hirano, *J. Appl. Phys.* **2001**, *89*, 1790.
[38] R. G. Kadam, A. K. Rathi, K. Cepe, R. Zboril, R. S. Varma, M. B. Gawande, R. V. Jayaram, *ChemPlusChem* **2017**, *82*, 467.
[39] D. P. Sahoo, S. Patnaik, D. Rath, B. Nanda, K. Parida, *RSC Adv.* **2016**, *6*, 112602.
[40] M. Selvaraj, B. H. Kim, T. G. Lee, *Chem. Lett.* **2005**, *34*, 1290.
[41] K. Sugiyama, H. Ishii, Y. Ouchi, K. Seki, *J. Appl. Phys.* **2000**, *87*, 295.
[42] A. J. Yun, J. Kim, T. Hwang, B. Park, *ACS Appl. Energy Mater.* **2019**, *2*, 3554.
[43] J. Tirado, C. Roldán-Carmona, F. A. Muñoz-Guerrero, G. Bonilla-Arboleda, M. Ralaiarisoa, G. Grancini, V. I. E. Queloz, N. Koch, M. K. Nazeeruddin, F. Jaramillo, *Appl. Surf. Sci.* **2019**, *478*, 607.
[44] V. Tunuguntla, W.-C. Chen, T. D. Newman, C.-Y. Chen, M.-C. Hsieh, S.-H. Lu, C. Su, L.-C. Chen, K.-H. Chen, *Sol. Energy Mater. Sol. Cells* **2016**, *149*, 49.
[45] H. Tsai, W. Nie, J.-C. Blancon, C. C. Stoumpos, R. Asadpour, B. Harutyunyan, A. J. Neukirch, R. Verduzco, J. J. Crochet, S. Tretiak, L. Pedesseau, J. Even, M. A. Alam, G. Gupta, J. Lou, P. M. Ajayan, M. J. Bedzyk, M. G. Kanatzidis, A. D. Mohite, *Nature* **2016**, *536*, 312.
[46] J. I. Kim, J. Kim, J. Lee, D.-R. Jung, H. Kim, H. Choi, S. Lee, S. Byun, S. Kang, B. Park, *Nanoscale Res. Lett.* **2012**, *7*, 482.
[47] T. Hwang, A. J. Yun, J. Kim, D. Cho, S. Kim, S. Hong, B. Park, *ACS Appl. Mater. Interfaces* **2019**, *11*, 6907.
[48] B. Lee, T. Hwang, S. Lee, B. Shin, B. Park, *Sci. Rep.* **2019**, *9*, 4803.
[49] M. Jung, Y. C. Kim, N. J. Jeon, W. S. Yang, J. Seo, J. H. Noh, S. I. Seok, *ChemSusChem* **2016**, *9*, 2592.

© 2019 The Authors. Published by WILEY-VCH Verlag GmbH & Co. KGaA, Weinheim